PHOTOREFRACTIVE PROPERTIES OF GALLIUM ARSENIDE AND SUPERLATTICES

Superlattices and multiple quantum wells have been studied intensively both experimentally and theoretically over the past 20 years (1). Because of the important optoelectronic applications of these structures, large emphasis has been placed on experimentally determining their optical properties. The two fundamental optical parameters of materials are the absorption coefficient α and the index of refraction n. The absorption coefficient $\alpha(\omega)$ is defined at each frequency ω as the relative rate of decrease in light intensity $I(\omega)$ along its propagation path in the material (2):

$$\alpha(\omega) = -\left[\frac{1}{I(\omega)}\right] dI(\omega)/dx \tag{1}$$

where x is the distance along this path. The index of refraction is defined as the ratio of the speed of light in vacuum c and in the material $v(\omega)$ at the same photon frequency ω:

$$n(\omega) = c/v(\omega) \tag{2}$$

Many applications of superlattices in laser optics are based essentially on the dispersion and optical wave-guiding properties of these structures which are directly related to the index of refraction (3–5). From a fundamental standpoint the optical properties are determined by the global dependence of the complex dielectric constant, $\epsilon(\omega) = \epsilon_1(\omega) + i\ \epsilon_2(\omega)$, where $\epsilon_1(\omega)$ and $\epsilon_2(\omega)$ are the real and imaginary parts, on the electronic structure of materials.

The absorption coefficient and refractive index are derived in terms of the complex dielectric constant as (6)

$$\alpha(\omega) = \frac{\omega\epsilon_2(\omega)}{nc} \tag{3}$$

and

$$n(\omega) = \sqrt{\frac{1}{2}\left[\epsilon_1 + \sqrt{\epsilon_1^2 + \epsilon_2^2}\right]} \tag{4}$$

which, because of small absorption at low frequency, i.e., ϵ_2 is small, gives $n(\omega) \approx \sqrt{\epsilon_1(\omega)}$. The real and imaginary parts of the dielectric function are given by Fermi's golden rule, which is based on the perturbation theory:

$$\epsilon_1(\omega) = 1 + \frac{8\pi e^2\hbar^2}{m_0\Omega} \sum_{\boldsymbol{k}_{\rm iv}\boldsymbol{k}_{\rm fc}} \frac{\left|\boldsymbol{\epsilon}.\boldsymbol{P}_{\rm cv}(\boldsymbol{k})\right|^2 \left[f_{\rm v}\left(E_{\boldsymbol{k}_{\rm iv}}\right) - f_{\rm c}\left(E_{\boldsymbol{k}_{\rm fc}}\right)\right]}{\left[E_{\boldsymbol{k}_{\rm fc}} - E_{\boldsymbol{k}_{\rm v}}\right]\left[\left(E_{\boldsymbol{k}_{\rm fc}} - E_{\boldsymbol{k}_{\rm iv}}\right)^2 - \hbar^2\omega^2\right]} \tag{5}$$

$$\epsilon_2(\omega) = \frac{4\pi^2 e^2}{m_0^2\omega^2\Omega} \sum_{\boldsymbol{k}_{\rm iv},\boldsymbol{k}_{\rm fc}} \left|\boldsymbol{\epsilon}.\boldsymbol{P}_{\rm cv}(\boldsymbol{k})\right|^2 \left[f_{\rm v}\left(E_{\boldsymbol{k}_{\rm iv}}\right) - f_{\rm c}\left(E_{\boldsymbol{k}_{\rm fc}}\right)\right] \delta\left[E_{\boldsymbol{k}_{\rm fc}} - E_{\boldsymbol{k}_{\rm iv}} - \hbar\omega\right] \tag{6}$$

where m_0 is the free electron mass, $\boldsymbol{\epsilon}$ is the polarization vector of the radiation, $f_{\rm c}$ and $f_{\rm v}$ are the electron and hole Fermi distribution functions in the conduction and valence bands with final and initial energies, $E_{\boldsymbol{k}_{\rm fc}}$ and $E_{\boldsymbol{k}_{\rm iv}}$, respectively, and Ω is the volume of the semiconductor. $\boldsymbol{P}_{\rm cv}$(k) is the momentum matrix element between final conduction electron states (fc) and initial valence hole states (iv) given by

$$\boldsymbol{P}_{\rm cv}(\boldsymbol{k}) = \langle \boldsymbol{k}_{\rm fc}\left|\hat{\boldsymbol{P}}\right|\boldsymbol{k}_{\rm iv}\rangle \tag{7}$$

where $\hat{\boldsymbol{P}}$ is the momentum operator and the electron wave function $|\boldsymbol{k}\rangle$ can be written as

$$\Psi_{\boldsymbol{k}}(\boldsymbol{r}) = \psi_{\boldsymbol{k}}(\boldsymbol{r})u_{\boldsymbol{k}}(\boldsymbol{r}) \tag{8}$$

where $u_{\boldsymbol{k}}(\boldsymbol{r})$ is a Bloch function which is periodic with the lattice constant, whereas $\psi_{\boldsymbol{k}}(\boldsymbol{r})$ is the envelope wave function, which varies slowly compared to the lattice constant. The interband matrix element can be approximated as

$$\boldsymbol{\epsilon} \cdot \boldsymbol{P}_{\rm cv}(\boldsymbol{k}) = M_{\rm b}M_{\rm env} \tag{9}$$

where $M_{\rm b}$ is the matrix element connecting the Bloch states near the band edge:

$$M_{\rm b} =< u_{\rm c}(\boldsymbol{r})|\boldsymbol{\epsilon} \cdot \boldsymbol{P}|u_{\rm v}(\boldsymbol{r}) > \tag{10}$$

while $M_{\rm env}$ is the overlap integral of the envelope wave functions between the valence and conduction bands:

$$M_{\rm env} = \int \psi_{\boldsymbol{k}\boldsymbol{c}}^*(r)\psi_{\boldsymbol{k}\boldsymbol{v}}(r)\, dr \tag{11}$$

The polarization of optical transitions enters into the model via the $M_{\rm b}$ factors. For quantum-well or superlattice structures, the symmetry is lowered by the layering along the z direction. Intraband transitions which are due to free carriers are not considered in this analysis.

The two parts of the dielectric function are related by the Kramers–Krönig relations which express the analyticity and the causality of $\epsilon(\omega)$:

$$\epsilon_1 = 1 + \frac{2}{\pi}\int_0^\infty d\omega'\, \frac{\omega'\epsilon_2(\omega')}{\omega'^2 - \omega^2} \tag{12}$$

$$\epsilon_2 = -\frac{2\omega}{\pi}\int_0^\infty d\omega'\, \frac{\epsilon_1(\omega) - 1}{\omega'^2 - \omega^2} \tag{13}$$

From Eq. (3) and Eq. (6), containing the energy conservation

J. Webster (ed.), *Wiley Encyclopedia of Electrical and Electronics Engineering*. Copyright © 1999 John Wiley & Sons, Inc.

δ-function, it is seen that the absorption coefficient is essentially determined by electron transitions between energy states separated by the photon energy $\hbar\omega$, whereas the index of refraction involving the real part $\epsilon_1(\omega)$ of the dielectric constant [Eq. (5)] is not restricted to such transitions. Consequently, while the absorption coefficient is restricted to a narrow energy range of the semiconductor spectrum, the index of refraction is determined by virtual transitions over the whole Brillouin zone.

As the computation of $\epsilon_1(\omega)$ and $\epsilon_2(\omega)$ requires the knowledge of the entire band structure of semiconductor materials, it is necessary to determine the wave functions and energy bands throughout the irreducible region of the first Brillouin zone.

$\boldsymbol{k \cdot p}$ METHOD AND BRILLOUIN-ZONE PARTITION

The entire band structure of specific semiconductors can be obtained with the $\boldsymbol{k \cdot p}$ technique by expanding about one symmetry point (8); however, this requires a large basis set and matrix Hamiltonian. In order to predict and to get physical insight into the optical properties of III–V compounds in general, it is desirable to have simple, analytical expressions for the energy bands and matrix elements. The hybrid $\boldsymbol{k \cdot p}$ model (9) which combines the advantages of the $\boldsymbol{k \cdot p}$ method with the generality of the pseudopotential method (10) achieves this objective. In this technique the band structure is generated by expanding the energies and wave functions about one or several symmetry points of the Brillouin zone. As the majority of low-energy optical transitions (i.e., $\hbar\omega < 6$ eV) originate from regions near the main symmetry points Γ, X, and L, $\boldsymbol{k \cdot p}$ expansions are carried out about three symmetry points, Γ, X, and L, by using a small number of bands in each of the $\boldsymbol{k \cdot p}$ basis sets, thereby limiting the accuracy of the energy-band expressions to regions surrounding the expansion points. Furthermore, because these are the highest symmetry points, it is mathematically straightforward to obtain expressions around these points, leading to a partition of the Brillouin zone (11). In the hybrid model, the $\boldsymbol{k \cdot p}$ band parameters are fitted empirically with experimental energy gaps and effective masses, when available; otherwise, these parameters are estimated from nonlocal pseudopotential calculations which include spin–orbit effects. Since the band parameters are fitted using experimental data, the $\boldsymbol{k \cdot p}$ method reproduces very accurately the band structure in the vicinity of the expansion points. Because of the size of the X and L regions, expansions about the K and W points supplement the X- and L-point expansions. However, because of the low symmetry characterizing these two points, it is difficult to obtain experimentally the energy dispersion relations and optical matrix elements in the volumes surrounding these points. Therefore, they are obtained directly from the pseudopotential calculations.

In order to evaluate the dielectric constant for energies less than 6 eV, it is reasonable to restrict the calculation to transitions between band-edge states where the transition rates are the largest. Consequently, in performing the energy expansions about Γ, X, and L, the band-edge states are treated exactly and the effects of the other bands (Löwdin states) are incorporated by using a perturbation technique described by Löwdin (12). The renormalizations are performed by including only those bands which give the largest contributions. This approximation results in a slight overestimation of the matrix elements involving these bands. In all of Löwdin states, it is often necessary to add d-symmetry states onto those states of Γ_{15} symmetry in order to obtain the correct energy-band curvatures. This idea was suggested by Chadi (13,14), who showed from pseudopotential calculations that there is appreciable mixing of d-symmetry states to an s–p basis set results in more accurate wave functions and energy bands.

Energy expansion about the Γ-point is given by Kane (8). For III–V compounds it is often assumed the energy dispersion is isotropic and renormalization involving the lowest Γ_{15} conduction states is only considered. The neglect of the Γ_1 valence state and the lowest Γ_{12} conduction states is reasonable because of the strength of the s–p wave-function interaction. The X- and L-point expansions have been discussed by Kane (8), Dresselhaus (15), and Kahen and Leburton (9).

EFFECTIVE MASSES

Table 1 lists the low-temperature (5 K to 77 K) values of the band-edge effective masses at the three symmetry points for the five III–V compounds (9). Presented are the longitudinal and transverse masses for the X and L states and the density-of-states masses for the Γ states. When experimental data are not available, the masses are calculated using the results of nonlocal pseudopotential calculations which include the spin–orbit interaction. These masses along with the energy gaps are used to determine the direct interaction and Löwdin coef-

Table 1. Low-Temperature Theoretical and Experimental Band-Edge Masses at the Γ, *X*, and *L* Symmetry Points

	GaAs	AlAs	InAs	InP	GaP
$\Gamma_1^c\ m^*$	0.067^a	0.140	$0.023^{b,c}$	0.077^b	0.122
$\Gamma_{hh}^v\ m^*$	-0.510^a	-0.536	-0.40^d	-0.58^e	-0.56^e
$\Gamma_{\ell h}^v\ m^*$	-0.082^a	-0.087	-0.026^d	-0.12^e	-0.16^e
$\Gamma_{so}^v\ m^*$	-0.154^a	-0.217	-0.166	-0.179	-0.289
$L_6^c\ m_\ell$	1.854	1.592	2.333	2.149	1.988
m_t	0.136	0.157	0.143	0.144	0.147
$L_{4,5}^v\ m_\ell$	1.731	2.011	1.668	2.021	1.948
m_t	-0.277	-0.290	-0.308	-0.295	-0.278
$L_6^v\ m_\ell$	1.731	2.011	1.668	2.021	1.948
m_t	-0.277	-0.290	-0.308	-0.295	-0.278
$X_7^c\ m_\ell$	0.495	0.385	0.593	0.566	0.551
m_t	0.258	0.254	0.305	0.279	0.249
$X_6^c\ m_\ell$	2.100	1.158	4.516	2.772	1.70^f
m_t	0.277	0.268	0.307	0.278	0.191^f
$X_7^v\ m_\ell$	1.209	1.300	1.236	1.341	1.258
m_t	-0.744	-0.659	-1.109	-0.839	-0.628
$X_6^v\ m_\ell$	1.209	1.300	1.236	1.341	1.258
m_t	-0.744	-0.659	-1.109	-0.839	-0.628

Each of the experimental masses is referenced. For Γ, only the density of states masses are given; while for X and L, both the longitudinal and transverse masses are presented.

[a] Reference 22.

[b] Reference 23.

[c] Reference 24.

[d] Reference 25.

[e] Reference 26.

[f] Reference 27.

ficients at the three symmetry points. Instead of taking the masses directly from the energy-band curvatures, a technique with a fair amount of uncertainty, the mass m^* at the point $\boldsymbol{k}_0$ is calculated using (8)

$$\frac{1}{m^*} = \frac{1}{m_0} + \frac{2\hbar^2}{m_0^2} \sum_{n'} \frac{|\boldsymbol{s} \cdot \nabla_{mn'}|^2}{E_n(\boldsymbol{k}_0) - E'_n(\boldsymbol{k}_0)} \tag{14}$$

where $\boldsymbol{s}$ is a unit vector in the direction of a principal axis, $\nabla_{nn'}$ is the gradient operator between the states n and n' at the point $\boldsymbol{k}_0$, and the summation is over all $n' \neq n$.

DIELECTRIC-CONSTANT FORMULATION

The dielectric constant is calculated as the sum of interband optical transitions. It is often sufficient to consider transitions between the highest valence-band states and the lowest conduction-band states. Consequently, for the Γ-region contribution, transitions between the upper three valence bands and the lowest conduction band are considered; for the X-region contribution there are transitions between the upper two valence bands and the two lowest conduction bands, and for the L-region contribution there are transitions between the upper two valence bands and the lowest conduction band. In Fig. 1, arrows on the GaAs band structure represent the aforementioned interband transitions. In the hybrid model both the L and X regions include the K and W points, even though Fig. 1 only shows the K point as being part of the X region.

In computing the dielectric constant, the summation over $\boldsymbol{k}$ states in Eqs. (3) and (4) is replaced by an integration over the first Brillouin zone. However, the integration is performed separately for each region around the Γ, X, and L points. The integration volumes for the Γ, X, and L regions are approximated by a sphere and two cones, respectively (see Fig. 2). For GaAs, the volumes of these regions, taking into account the sixfold and eightfold degeneracies of the X and L regions, respectively, are 8.24×10^{-2} Å^{-3}, 1.35 Å^{-3}, and 4.01 Å^{-3}, for Γ, X, and L, respectively. The total volume of 5.44 Å^{-3}, is less than 1% different from the actual volume of the first Brillouin zone of GaAs.

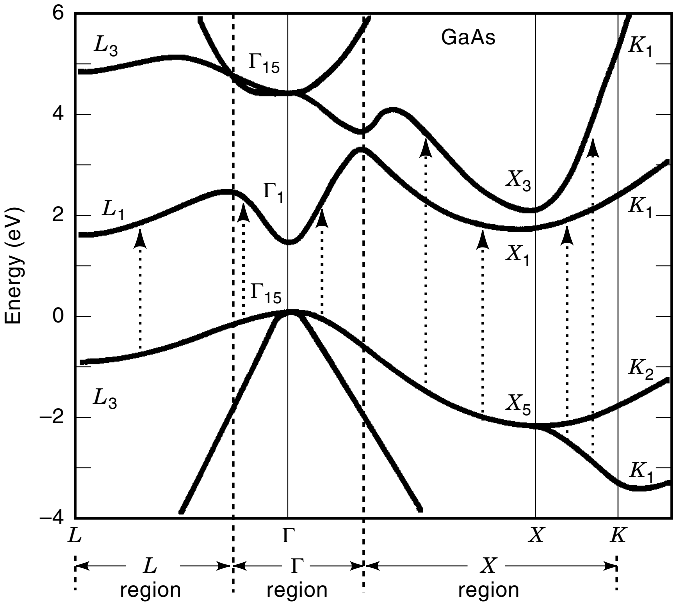

Figure 1. Optical transitions between the band-edge valence and conduction bands for the three regions, Γ, X, and L, for GaAs. Only these transitions are included in the hybrid model.

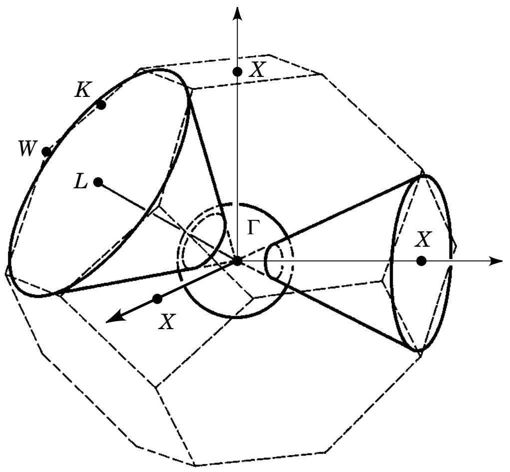

Figure 2. Partition of the first Brillouin zone of a zinc-blended lattice into the G, X, and L regions. The G region is a sphere, while the X and L regions are both cones. The K and W points are also part of the X region.

The integrations over the X and L regions are performed by taking into account the anisotropy of the two regions into the hybrid model in the $\boldsymbol{k} \cdot \boldsymbol{p}$ expansions from both points toward the Γ, K, and W points. By using the results of nonlocal pseudopotential calculations, analytical expressions for expansions from K and W toward the Γ, K, and L points can be obtained; the energies and matrix elements between the expansion lines can be computed by linear interpolation, which, in spite of its roughness, yields reasonable results.

Figure 3 shows the $\epsilon_2(\omega)$ curves obtained by the hybrid model and compared with the experimental data of Aspnes and Studna (16). Because the theoretical curves have been generated by using low-temperature (5 K) band-structure data, the experimental data which are obtained at 300 K have been shifted by 0.1 eV in order to account for this temperature difference. Experimental data do not exist for AlAs. The most noticeable feature of all of the curves is the presence of the two well-known E_1 and E_2 peaks. The E_1 peak arises from transitions occurring over a large portion of the Brillouin zone around the L points. There is no E_1 peak for AlAs because the L- and K-point energy gaps differ by less than 1 eV; hence, the position of the AlAs E_1 peak overlaps with the low-energy slope of its E_2 peak. Except for InAs and GaAs for which the theoretical curves show a small structure due to the L-point spin–orbit splitting, the Ga and In compounds exhibit unsplit E_1 peaks which are broader than the experimental peaks. This is mainly due to the absence of exciton effects in the hybrid model. Exciton effects might have various consequences on the magnitudes of the E_1 peaks because they alter both the density of states and the optical matrix elements. According to Velicky and Sak (17) and Hanke and Sham (18), excitons should sharpen and enhance the E_1 peak. Without

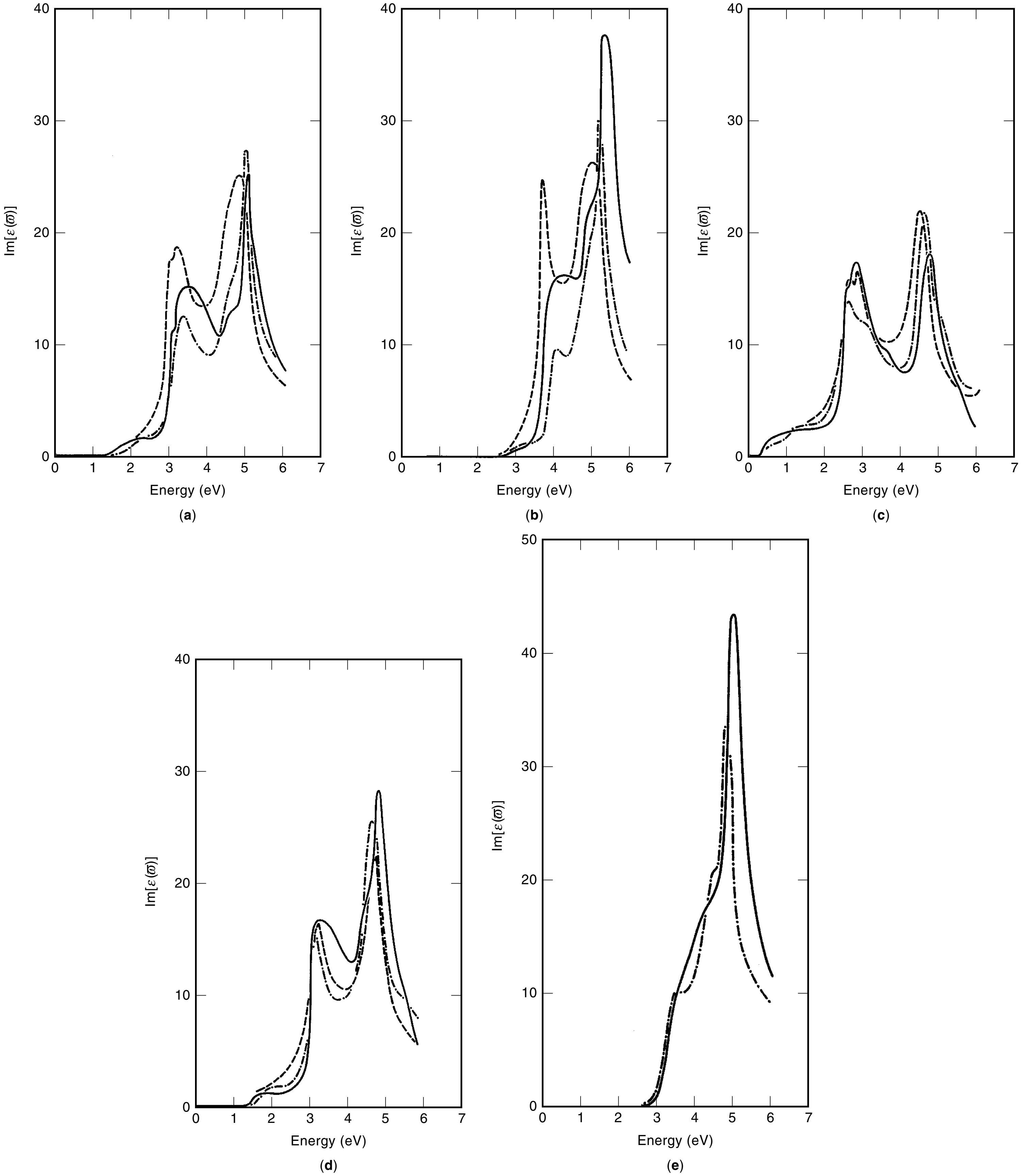

(a) (b) (c) (d) (e)

Figure 3. Imaginary part of the dielectric constant of five III–V compounds. The solid and dotted–dashed lines are calculated by the $\boldsymbol{k}\cdot\boldsymbol{p}$ and nonlocal pseudopotential methods, respectively, while the dashed line is the experimental results. (a), (b), (c), (d), and (e) are for GaAs, GaP, InAs, InP, and AlAs, respectively. The experimental data are extrapolated to 5 K.

excitons, the E_1 peak arises from transitions away from the L–Γ line because the band-edge conduction and valence bands along that line have small transverse masses and, correspondingly, small densities of states which are insufficient to support a peak. Consequently, the peak is shifted to higher energies where the phase space is larger. Exciton effects should lower the L gap and raise the transverse effective masses, resulting in higher densities of states along the L–Γ line. Thus, the structure of the line would be reflected in the shape of the E_1 peak, that is, the peak would become split.

This argument is corroborated by the theoretical model: The InAs band-edge matrix elements are a factor of 2 smaller than those of GaP; however, InAs has the largest E_1 peak. Furthermore, its peak is the sharpest and the most centered of the four compounds. This occurs because its transverse energy-band curvature is the smallest among these compounds; hence, the E_1 peak is supported mainly by transitions occurring close to the L–Γ line.

The E_2 peak originates from a region around the special $\boldsymbol{k}$ point ($\frac{3}{4}$, $\frac{1}{4}$, $\frac{1}{4}$) as suggested by Aspnes (19) and computed by Chelikowsky and Cohen (20). Indeed, the density of states in this region is more important than the magnitude of the optical matrix elements in influencing the strength of the E_2 peak. Excitons should lower the E_2 peak (17,18). A possible explanation is that excitons could disrupt the parallel-band curvature in the vicinity of the special $\boldsymbol{k}$ point. This would lower the effective density of states in this region and, consequently, reduce the E_2 peak. The same exciton effect can account for the slight energy difference between the experimental and theoretical curves for GaAs, GaP, InAs, and InP.

The other regions of the Brillouin zone have small contributions to the dielectric constant in the 0 eV to 6 eV range. The Γ-valley contribution is negligible because of its small phase space as shown before. The X-region contribution is small because its phase space and matrix elements are, respectively, about a factor of 3 and 2 smaller than those of the L region.

COMPARISON WITH PSEUDOPOTENTIAL

Figure 3 also compares the results of the hybrid model with those generated by a nonlocal pseudopotential calculation. The spin–orbit interaction is not included in the pseudopotential calculations. For GaP, the effect of the omission is negligible; however, for the other four compounds, the spin–orbit interaction effectively lowers the important band gaps by ~0.1 eV. Consequently, for these four compounds, the $\epsilon_2(\omega)$ curves have been shifted so that the L-point energy gaps agree with the spin–orbit results. From $\boldsymbol{k} \cdot \boldsymbol{p}$ theory, it can be shown that this is a good approximation since the spin–orbit interaction only shifts the bands, having a small effect on the band curvatures and matrix elements at L, X, and K (8).

The results of the hybrid model compare favorably with both the experimental and pseudopotential results. The magnitudes of our E_1 peaks are larger and more closely approximate the experimental peaks than those determined by the pseudopotential calculations. For GaAs, InAs, and InP, the E_2 peaks calculated by the $\boldsymbol{k} \cdot \boldsymbol{p}$ and pseudopotential methods are comparable in magnitude, but slightly shifted with respect to the experimental E_2 peaks, while for AlAs and GaP the $\boldsymbol{k} \cdot \boldsymbol{p}$ peaks are substantially larger than the pseudopotential peaks. The discrepancy in the magnitudes of the E_1 and E_2 peaks calculated by the $\boldsymbol{k} \cdot \boldsymbol{p}$ and pseudopotential methods can be attributed to the difference in the values of the optical matrix elements and to the linear interpolation approximation of the off-expansion line energies as discussed previously. As mentioned above, the $\boldsymbol{k} \cdot \boldsymbol{p}$ matrix elements involving the Löwdin states are overestimated due to the neglect of all but the closest higher bands of the proper symmetry. However, the band-edge $\boldsymbol{k} \cdot \boldsymbol{p}$ and pseudopotential matrix elements differ by only a few percent. This result agrees with the calculation of Hermann and Weisbuch (21), who found that the Γ-point band-edge matrix elements are insensitive to the higher-band contributions. Since the band-edge matrix elements determine the low-frequency dielectric constant, the discrepancy in the peaks is, therefore, largely the result of our linear interpolation approximation. The problem with this approximation is that although it provides a good average energy dispersion relation, it sometimes produces a poor value for the density of states. This discrepancy also accounts for the difference in the shapes of the two curves. Nevertheless, despite the approximations involving the matrix elements and energy dispersion relations, the results of the two models are comparable for GaAs, InAs, and InP and assert the validity of our model.

THE ZERO-FREQUENCY DIELECTRIC CONSTANT: $\epsilon_1(0)$

Table 2 gives the electronic contribution to the real part of the dielectric constant at low frequency $\epsilon_1(0)$ at 5 K for the five III–V compounds. Also listed are the experimental values and the individual contributions of the three regions. Only

Table 2. Theoretical and Experimental $\epsilon_1(0)$ Values at 5 K for Five III–V Compounds[a]

Material	$\epsilon_1(0)$ Theory	$\epsilon_1(0)$ Experimental	Percent Error	Contributions of the Three Regions L	X	Γ
GaAs	8.68	10.60	18.1	6.01	1.25	0.41
AlAs	7.42	7.90	6.1	5.12	1.16	0.14
InP	9.13	9.27	1.5	6.68	1.12	0.33
InAs	10.10	11.49	12.1	7.26	0.94	0.91
GaP	8.77	8.80	0.4	6.30	1.21	0.25

[a] Also included are the calculated individual contributions of the Γ, X, L regions to $\epsilon_1(0)$ for each of the five compounds.

the GaAs experimental data are 5 K values; for the other four materials the values are extrapolated from 300 K by using the GaAs $\epsilon_1(0)$ temperature dependence. The theoretical values are uniformly low with an average error of ~7.5%. The error is partly due to the omission of all high-energy transitions. The errors for AlAs, InP, and GaP are small because of the overestimation of the virtual transitions corresponding to the E_2 peak. This effect is particularly pronounced for GaP where the E_2 transitions compensate for the small contribution from the E_1 transitions. For GaAs, the error results also from its weak E_1 contribution. For InAs the error is ~12% in spite of its large E_1 peak. This probably stems from the fact that its E_2 peak is small and $\epsilon_1(0)$ of this small gap material is affected most by the neglect of higher-band contributions in the hybrid model.

The valley contributions are split up according to the partition of the Brillouin zone as presented previously. For all materials, the L region contributes approximately 60% to 70% to the total value of the dielectric constant while the Γ region accounts for about 5% to 10%. This general trend is also confirmed for optical frequencies corresponding to the Γ energy gap. Thus, the index of refraction is essentially determined by the band structure away from the center of the Brillouin zone. The implications of these results are important for complex materials and superstructures, where the modifications of the electronic structure at L and X, rather than at Γ, produce the variations in the index of refraction. An additional consequence of these results is a better understanding of the validity of the Penn model (22). The latter is based on a three-dimensional (3D), nearly free-electron, band model. The Brillouin zone is approximated as a sphere and the band edges are displaced from the center to the surface of the zone, resulting in a singular density of states around the band gap. Penn pointed out that such a singular behavior in a 3D system would not appear if the gap is placed at the center of the zone. It is the fortuitous coincidence of this singular density of states at the edge of the zone with the actual description of the states around the L and K points, characterized by large interband matrix elements and densities of states, which provides the Penn model with its validity and success in calculating the dielectric constant.

SUPERLATTICE ELECTRONIC STRUCTURE

Superlattices are artificial structures made of thin alternating layers of semiconductor materials of different compositions such as GaAs/AlAs. In long-period superlattices the periodic variation of the band gap produces quantization of the electronic states which results in the formation of minibands which are superimposed upon the bulk band structure of the constituent materials. We account for this band modulation by quantizing the z component of the wave vector $\boldsymbol{k}$ which results in a superlattice wave function of the form

$$\Psi_k = e^{i\boldsymbol{k}_\parallel \cdot \boldsymbol{r}_\parallel} \Phi^j_{K_z}(z)|b> \tag{15}$$

where K_z is the superlattice traveling wave vector in the z direction, $\boldsymbol{r}_\parallel$ and $\boldsymbol{k}_\parallel$ are the position coordinate and wave vector in the plane parallel to the superlattice layers, $|b\rangle$ is the periodic part of the bulk Bloch state, and $\Phi^j_{K_z}(z)$ is the superlattice envelope wave function of the jth quantized state whose periodic part is found from the solution of the coupled square-well potential. In this approximation it is assumed that the superlattice periodicity acts only upon the envelope wave function in the z direction. Therefore, the periodic part of the Bloch wave function is unchanged from its bulk value and is determined using a $\boldsymbol{k}\cdot\boldsymbol{p}$ band calculation described above. Consequently, the superlattice band structure differs from the corresponding bulk material band structure only in the quantization direction. This appears to be a reasonable approximation, as will be shown by the good agreement between the theoretical results and the experimental data later on. The following simplified expression for the energy dispersion relation of the minibands in the z direction is assumed (23):

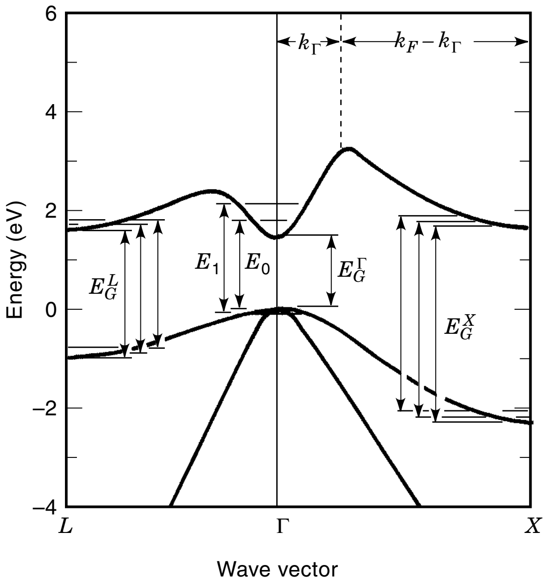

Figure 4. Band structure of GaAs and the effect of quantization on each of the symmetry points.

$$E_j(K_z) = E_j + (-1)^j W_j \cos(K_z d) \tag{16}$$

where E_j and W_j are the midband energy and energy width of the jth miniband, respectively, and d is the period of the superlattice. The superlattice miniband energy dispersion relation $E^j_{\mathrm{SL}}(k_x, k_y, K_z)$ is calculated by adding Eq. (16) onto the bulk relation $E_{\mathrm{B}}(k_x, k_y, k_z)$ and quantizing the k_z wave vector. The superlattice optical matrix element M_{SL} between the valence and conduction bands is obtained by quantizing the z component of the $\boldsymbol{k}$ vector in the bulk matrix-element expression M_b, which is obtained from previous calculations, Eq. (10). Hence,

$$\begin{aligned} E_{\mathrm{B}}(k_x, k_y, k_z) &\to E^j_{\mathrm{SL}}(k_x, k_y, K_z) \\ &= E_{\mathrm{B}}(k_x, k_y, k_j) + \Delta E_j + (-1)^j W_j \cos(K_z d) \end{aligned} \tag{17}$$

$$M_b(k_x, k_y, k_z) \to M_{\mathrm{SL}}(k_x, k_y, k_j) \tag{18}$$

Here ΔE_j is the shift in the energy of the jth level resulting from the carrier confinement. The values of W_j and ΔE_j are determined using the interface-connection rules described below and $k_j = [2(j-1)+1]\ \pi/2d$. By applying Eqs. (17) and (18) at the three symmetry points, Γ, K, and L, we obtain the quantized electronic band structure presented in Fig. 4. Since

K and W are low-symmetry points, the effects of quantization are negligible for the contributions coming from these regions. Therefore, these contributions are treated in a mean-field approximation where the energy and matrix-element dispersion relations are approximately equal to the compositionally averaged bulk alloy values. The alloy values are calculated using the virtual-crystal approximation (VCA) (24).

INTERFACE-CONNECTION RULES

The envelope wave function $\Phi^{i}_{K_z}(z)$ and the quantization of the z component of the $\boldsymbol{k}$ vector are obtained through the use of connection rules across the interfaces of the superlattice square-well potentials by assuming continuity of the entire wave function and its derivative at the interfaces (25). However, since the GaAs–$Al_xGa_{1-x}As$ junction is not abrupt, these relations are averaged over the volume of a crystal unit cell. After carrying out these averages, the usual connection rules of the continuity of $F(z)$ and $[1/m(E)]/(dF(z)/dz)$ across the interface, where F is the envelope wave function and $m(E)$ is the energy-dependent mass of a specific band, are recovered. Here the z direction is perpendicular to the interface and the mass $m(E)$ is given by

$$\frac{1}{m(E)} = \frac{1}{m_0}\left[1 + \frac{\left\langle b_k \left| \frac{d}{dz} \right| b_k \right\rangle}{ik_z(E)}\right] \tag{19}$$

where $k_z(E)$ is the bulk energy-dependent wave vector, and $|b_k\rangle$ is the bulk cell periodic wave function obtained using the results of the $\boldsymbol{k}\cdot\boldsymbol{p}$ expressions discussed previously. Thus, the interface-connection rules are based on the envelope-function approximation (26). The advantage of this method is that it incorporates the nonparabolicity of the band structure while the simplicity of the square-well potential (Kronig–Penney picture) is preserved. The drawback is that mixing effects between valence-band states as well as between Γ–X and Γ–L symmetry states in the conduction band are neglected. The former is responsible for the fine structure in the absorption coefficient (27) and will be ignored in this approach.

By applying the energy-dependent connection rules to a periodic superstructure, the relations are analogous to that of Sai-Halasz et al. (26), except that now the masses that are energy-dependent are obtained:

$$\cos(K_z d) = \cos(k_z^A L_z)\cos(k_z^B L_B) - Q\sin(k_z^A L_z)\sin(k_z^B L_B) \tag{20}$$

$$Q = \frac{1}{2}\left[\frac{k_z^A m_B(E)}{k_z^B m_A(E)} + \frac{k_z^B m_A(E)}{k_z^A m_B(E)}\right] \tag{21}$$

Here L_Z and L_B are the well and barrier widths of materials A and B, respectively, $d = L_Z + L_B$, and k_z^A and k_z^B are the energy-dependent wave vectors of Eq. (19). In order to evaluate Eqs. (20) and (21), it is necessary to determine the energy-band offsets at the Γ, X, and L symmetry points. Figure 5 gives the offsets for a GaAs–AlAs interface at 300 K assuming a 65 : 35 Γ-point band discontinuity ratio. The energy levels in Fig. 5 are obtained using experimental data, when available; otherwise, they are estimated from nonlocal pseudopotential calculations which include spin–orbit effects.

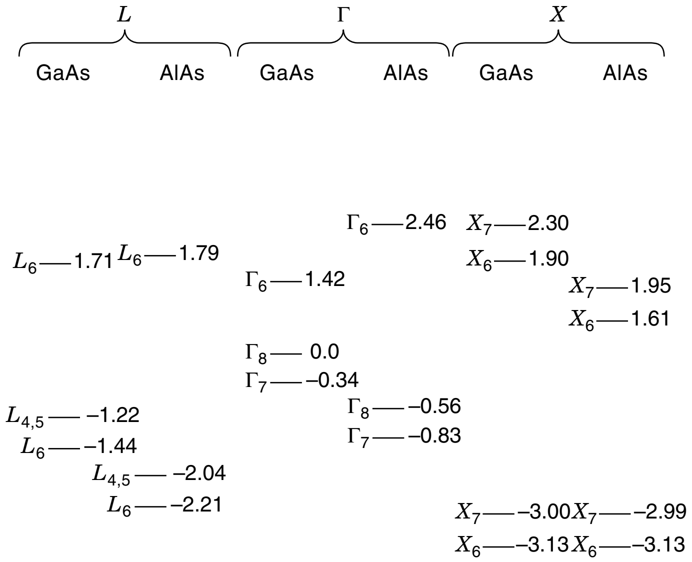

Figure 5. Energy-band offsets at 300 K at each of the symmetry points for a GaAs–AlAs superlattice. The energy levels are calculated assuming a 65 : 35 Γ-point band-discontinuity ratio. Each level is marked with the appropriate double-group-symmetry notation.

For absorption due to excitons, there is a bound $\epsilon_2(\omega)$ contribution and a continuum $\epsilon_2(\omega)$ contribution. The bound $\epsilon_2(\omega)$ contribution is given by (27,28)

$$\epsilon_{2,B}(\omega) = \frac{Cf_0\gamma}{\pi[(E-E_0)^2+\gamma^2]} \tag{22}$$

$$f_0 = |U(\boldsymbol{r}=\boldsymbol{0})|^2|\epsilon\cdot\boldsymbol{P}_{\text{cv}}(0)|^2 \tag{23}$$

where the bound-exciton peaks is described by a Lorentzian function with an oscillator strength f_0 and a half-width γ, C is a constant factor, and E_0 and $U(r)$ are the ground-state exciton energy and envelope function, respectively (the bound excited states are ignored). Both E_0 and $U(r)$ are calculated using a variational exciton model of Greene et al. (29). This exciton model is implemented for periodic superstructures by having all of the parameters material- and energy-dependent. The ground-state exciton binding energies are calculated by subtracting from the variational energies the energies resulting from Eqs. (20) and (21).

For the continuum contribution, a two-dimensional exciton model (30,31) yields

$$\epsilon_{2,C}(\omega) = \epsilon_{2,F}(\omega)\frac{e^{\pi\alpha}}{\cosh(\pi\alpha)} \tag{24}$$

$$\alpha = \left[\frac{R}{\hbar\omega - E_0}\right]^{1/2} \tag{25}$$

where $\epsilon_{2,F}(\omega)$ is the value of the free carrier $\epsilon_2(\omega)$ without the electron–hole interaction, assuming a constant value for $\boldsymbol{P}_{\text{cv}}(\boldsymbol{k})$, and R is the effective exciton Rydberg. The exciton model outlined above is a good approximation for strong potential barriers (large barrier width and heights) and small well thicknesses (29).

RESULTS AND DISCUSSION

The absorption coefficient of a GaAs–$Al_{0.5}Ga_{0.5}As$ superlattice with a well and barrier thickness of 85 Å and 80 Å, respectively, is plotted in Fig. 6. The results are given for light being polarized parallel to the superlattice layers. The solid and dotted–dashed lines are the theoretical and experimental (3) values, respectively. The arrows indicate the quantized Γ-point valence-band–conduction-band transitions which produce the fine structure on the theoretical curve. Since the experimental data have arbitrary units, the data are multiplied by a constant factor such that the two second electron–heavy-hole peaks, $E_2(e\text{–hh})$, coincide. The values of γ which are used to fit the five main peaks are ~1, 1, 3, 3, and 9 meV, respectively, while the calculated binding energies E_0 are ~10, 10, 11, 11, and 14 meV, respectively. As can be seen from the figure, the peak positions agree reasonably well with the experimental data, with the only discrepancy stemming from the $E_2(e\text{–lh})$ peak (lh denotes light hole). The error results from the use of bulk masses in the plane parallel to the layers. Since a different mass would change both the binding energy and the continuum position, it is difficult to ascertain qualitatively the overall effect. The sharp rise in the experimental curve for energies greater than ~1.75 eV is due to an experimental artifact (32). Overall, this figure demonstrates the flexibility of our dielectric-constant model and shows the accuracy of our interface-connection rule and exciton-binding-energy models.

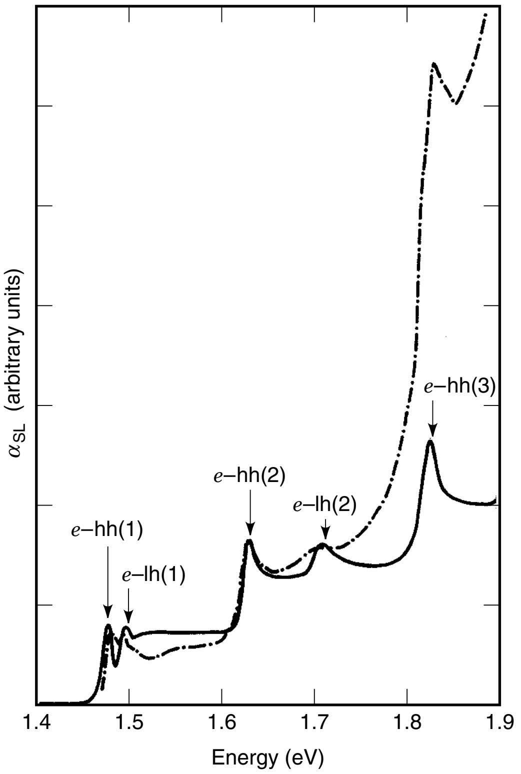

Figure 6. Relative absorption of GaAs–$Al_{0.5}Ga_{0.5}As$ superlattice for parallel polarization at 300 K. The solid and dotted–dashed lines are the theoretical and experimental values, respectively. The arrows mark the positions, relative to the theoretical curve, of the Γ-valley transitions. e–hh(j) corresponds to a transition between the jth level of the heavy-hole band and jth level of the lowest conduction band. L_Z = 85 Å, L_B = 80 Å.

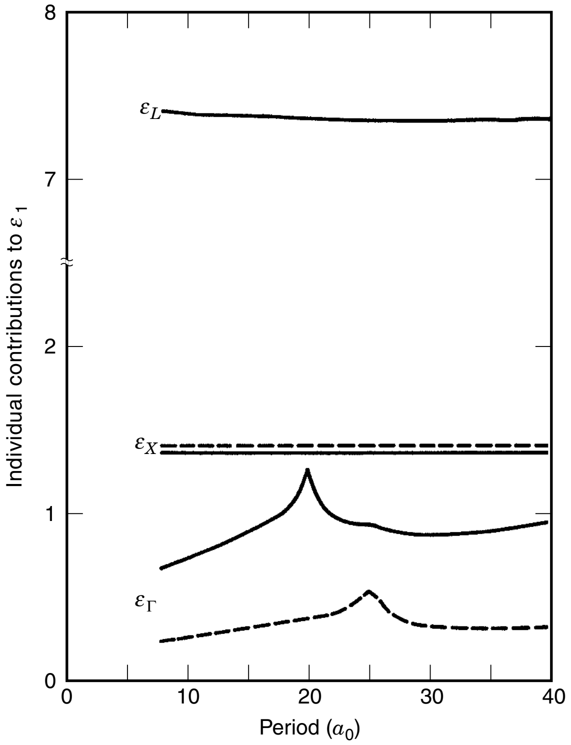

Figure 7. Structure dependence of the Γ, X, and L region contributions to the real part of the dielectric constant of a GaAs–AlAs superlattice at $\hbar\omega$ = 1.5 eV. The mole fraction of AlAs in the structure is $\bar{x} = L_B/L_B + L_Z = 0.3$ and a_0 is the lattice constant. Solid line: Electric field polarization vector parallel to the superlattice layers. Dashed line: Electric fields polarization vector perpendicular to the superlattice layers. Note that the L-region contribution is isotropic.

Figure 7 gives the contributions of the Γ, K, and L regions to the real part of the dielectric constant of a GaAs–AlAs superlattice at $\hbar\omega$ = 1.5 eV for the light being polarized parallel and perpendicular to the superlattice layers (solid and dashed lines, respectively). Values are presented as a function of the period $d = L_B + L_Z$ for a mole fraction $\bar{x} = L_B/(L_Z + L_B)$ of AlAs of 0.3. The superlattice quantization axis is in the [100] direction. Notice the large L contribution with respect to the Γ and X contributions. This results from the combined effects of large densities of states and momentum matrix elements and small energy gaps present in the L region (9). The largest contributions come from volumes surrounding the L point and a special $\boldsymbol{k}$ point at $(\frac{3}{4}, \frac{1}{4}, \frac{1}{4})$. The X valley also has a high density of states; however, its phase space and matrix elements are appreciably smaller than those of the L valley (9). The L contribution is approximately independent of the period because the superlattice quantization axis is not aligned with any of the principal axes. Hence, in agreement with the experimental findings of Laidig et al. (33), the effect of the superstructure is only weakly felt at L. The L contribution is isotropic since the x, y, and z directions are all equivalent for the [111] direction. Therefore, for a superlattice grown along the [100] direction, the polarization of the L valleys, as an average over the three orthogonal directions, vanishes in analogy to the bulk case.

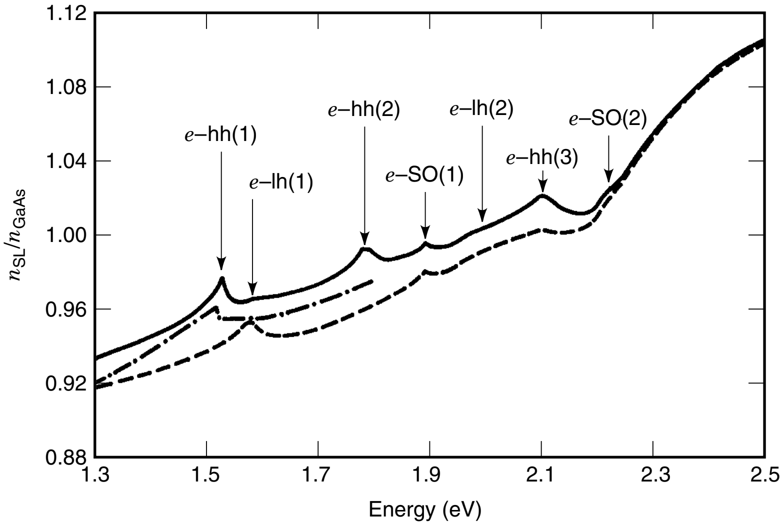

Figure 8. Normalized index of refraction of a GaAs–AlAs superlattice as a function of frequency. The solid and dotted–dashed lines are the theoretical and experimental parallel polarization values, respectively, and the dashed curve give the theoretical perpendicular polarization values. The arrows mark the positions of the quantized Γ-valley transitions. e–hh(j) corresponds to a transition between the jth level of the heavy-hole band and the jth level of the lowest conduction band. L_Z = 62 Å, L_B = 27 Å.

The Γ and X contributions both increase as a function of the period. The superlattice structure influences the dielectric constant by determining both the position and miniband width of the lowest quantized energy levels. Each are inverse functions of L_B and L_Z. It can be easily determined that the miniband widths have a negligible effect on the dielectric constant. Therefore, the important factor is the lowering of the quantized levels which results in an increase in ϵ_1 with the period. The peaks on the parallel Γ-polarization curve correspond to the first electron–heavy-hole and electron–light-hole transitions, $E_1(e\text{–hh})$ and $E_1(e\text{–lh})$, respectively. For the perpendicular polarization, only $E_1(e\text{–lh})$ is present since the symmetry of the heavy-hole state precludes momentum matrix elements in the quantization direction. Polarization effects at Γ occur because the heavy-hole transitions which are responsible for the strong coupling between the Γ conduction and valence bands are absent for perpendicular polarization.

The X contribution is a weak function of the period because only the conduction band is quantized (the very small offset between the two valence bands could be ignored as shown in Fig. 5), and, in comparison with the Γ-point conduction-band mass, both the transverse and longitudinal conduction band masses are large and, thus, rather insensitive to the confinement. Hence, in this case, the dielectric constant assumes approximately its bulk alloy value. For the X region the optical matrix elements are also appreciable only for light polarized along the x and y directions—that is, similar to the e–hh transition. However, two of the valleys have the superlattice quantization axis parallel to the z component of the optical matrix elements while the other four valleys have the quantization axis aligned along the y component of the matrix element. Hence, perpendicular polarization (the quantization axis is perpendicular to the layers) is favored by four of the six X valleys, which accounts for the reverse polarization trend for the X-valley contribution.

In Fig. 8 the theoretical results for the normalized index of refraction of a GaAs–AlAs superlattice are compared with the experimental data of Suzuki and Okamoto (4). The calculated data are for parallel and perpendicular polarization (solid and dashed line), respectively, while the experimental data are for parallel polarization (dotted–dashed line). The superlattice has a well and barrier thickness of 62 Å and 27 Å, respectively, and, consequently, $\bar{x}$ = 0.3. The experimental data only go up to $\hbar\omega$ = 1.8 eV. Because of the restriction to interband transitions smaller than 6 eV in the hybrid model, the results for the bulk GaAs index of refraction are ~7% smaller than the experimental values (34). For most optical transitions, the influence of the higher bands can be accounted for by a constant factor. In Figs. 8 and 9, the theoretical and experimen-

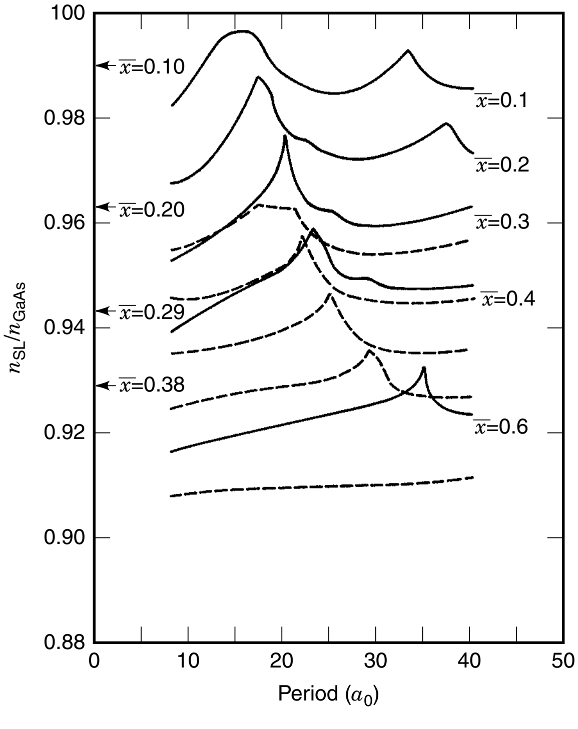

Figure 9. Structure dependence of the normalized index of refraction at 1.5 eV for a number of GaAs–AlAs superlattice structures. The solid and dashed lines are for light being polarized parallel and perpendicular to the layers, respectively, and a_0 is the lattice constant. The arrows on the left-hand side of the figure mark the positions of the normalized experimental alloy values for the indicated mole fractions $\bar{x}$ of Al. The mole fractions given on the right-hand side of the figure belong to the adjacent parallel–polarization curve, whereas for perpendicular polarization the indicated mole fractions correspond to the curves in descending order. $\bar{x} = L_B/L_B + L_Z$, 300 K.

tal $n(\omega)$ values given have been renormalized with respect to the theoretical and experimental bulk GaAs index of refraction values at $\hbar\omega = 1.5$ eV, respectively, to account for this constant contribution. As in Fig. 5, the theoretical parallel polarization curve is labeled according to the appropriate quantized Γ-region transitions. The peaks on the theoretical perpendicular polarization curve are the result of the corresponding light-hole and split-off-hole transitions indicated on the parallel-polarization curve. As discussed previously, there are no heavy-hole transitions for perpendicular polarization and the dielectric constant is larger for parallel polarization. However, it should be pointed out that the anistropy vanishes around 2.3 eV due to the falling off of the Γ contribution and the isotropy of the L contribution.

The theoretical results compare favorably with the experimental data, there being less than a 2% discrepancy between the two parallel polarization curves. The calculated $E_1(e\text{–hh})$ peak is shifted to higher energies by ~8 meV and is slightly larger. The slight shift may result from the uncertainties in the AlAs band-structure parameters; and in the Γ-point band-discontinuity ratio (35), both the $E_1(e\text{–lh})$ and $E_2(e\text{–hh})$ peaks are absent from the experimental data. The light-hole transitions are barely noticeable on the calculated parallel-polarization curve, being weak and overshadowed by the neighboring e–hh transitions. It is not known why the $E_2(e\text{–hh})$ peak is absent from the experimental data. However, in general the experimental data verify the validity of the superlattice model.

In Fig. 9 we show the normalized index of refraction at 1.5 eV for a range of GaAs–AlAs superlattices. Again, the solid and dashed lines are for light being polarized parallel and perpendicular to the superlattice layers, respectively. Also shown in the figure are the normalized experimental alloy values (34) corresponding to four of the five superlattice compositions (there are no data for $\bar{x} = 0.6$). As in Fig. 8, the main peaks on the curves correspond to the quantized Γ-region transitions. All of the parallel-polarization curves exhibit the $E_1(e\text{–hh})$ peak, while the $\bar{x} = 0.1$ and 0.2 curves also show the $E_2(e\text{–hh})$ peak. Again, for perpendicular polarization the peaks are due to the $E_1(e\text{–lh})$ transition. The $E_1(e\text{–lh})$ transition also contributes to the parallel curves; however, it is barely noticeable, being overshadowed by the neighboring $E_1(e\text{–hh})$ peak as in the previous figure. For both polarizations the peaks become larger and narrower up to $\bar{x} = 0.3$, after which they become smaller. These effects can be explained by the following mechanisms. For small $\bar{x}$ values the peaks are broad because a large change in the period is required to modify the superlattice characteristics which resemble those of bulk GaAs. Additionally, the effects of quantization are weakly felt for these structures which results in shallower peaks. For larger $\bar{x}$ values, the superlattice properties are a stronger function of the period which produces sharper peaks; however, with increasing AlAs content, the peaks become shallower because the AlAs Γ-region contribution is approximately a factor of 7 times smaller than that of GaAs (9).

A characteristic feature of all of the curves is the shift in the peak positions for increasing AlAs content. For any mole fraction $\bar{x}$, the energy of an optical transition increases as a function of the barrier width, but decreases more rapidly with the well width; consequently, the transition energies are the largest for small period superlattices because of the strong confinement. Therefore, as the period d increases for constant $\bar{x}$, the transition energy decreases (weakening confinement since L_Z increases) and a peak occurs when the energy crosses the 1.5 eV level. Also, as $\bar{x}$ increases for a constant value of the period, the transition energy increases since L_B is increasing while L_B is decreasing (AlAs has a larger band gap than GaAs). Therefore, larger L_Z values (i.e., the shift in the peaks for increasing $\bar{x}$) are required to reduce the transition energy to the value of 1.5 eV. This explains why the curves with the smallest barrier values, $\bar{x} = 0.1$ and 0.2, also contain the $E_2(e\text{–hh})$ transition, and why the $\bar{x} = 0.6$ curve for perpendicular polarization does not exhibit the $E_1(e\text{–lh})$ transition.

Another feature of the curves is the strong polarization effect which weakens with increasing AlAs content. Parallel polarization is favored since the superlattice Γ contribution is more anisotropic than the X contribution. The reduction in anisotropy occurs because of the smaller AlAs Γ-region contribution, as explained previously.

The most important point to notice in Fig. 9 is the positions of the alloy index-of-refraction values relative to those of the superlattices. For parallel polarization it can be seen that the difference between the alloy and superlattice index of refractions increases with $\bar{x}$ and with L_B—that is, with the period. The latter trend is in agreement with the experimental findings of Suzuki and Okamoto (4) and confirms the conjecture of Holonyak et al. (5) about the difference in the index of refractions of a superlattice and its corresponding alloy. Figure 9 also shows that this difference is largest at the quantized transition energies and can be as high as ~3.5% for specific superlattice structures. In calculations, an optimal value is achieved for a structure characterized by $L_Z \approx 79$ Å and $L_B \approx 40$ Å. However, because the hybrid model overestimates $n(\omega)$ by ~1.5% with respect to the experimental superlattice values, a more accurate estimate of the difference between the index of refractions of the two structures is ~2%. Optical wave-guiding can already occur using an index step of ~0.0063 (assuming a symmetric AlGaAs planar wave guide with a thickness of 2 μm and $\hbar\omega = 1.5$ eV) (36), whereas here we show that with certain structures a step of ~0.07 (i.e., a factor of 10 larger) can be obtained. Consequently, the wave-guiding and reflectance properties of optoelectronic devices which incorporate superlattices are drastically improved by tailoring the structure to the chosen optical frequency.

EXCITON EFFECTS IN THE INDEX OF REFRACTION OF QUANTUM WELLS AND SUPERLATTICES

Because of the quasi-two-dimensional character of the excitons in quantum wells exciton resonances are clearly observable at room temperature. For both the bound and continuum contributions to the exciton (see Eqs. 22–25), the polarization of the optical excitation enters into the model via the $|\boldsymbol{\epsilon}\cdot\boldsymbol{P}_{cv}|^2$ factor. For bulk materials, on account of their isotropy, this factor is equal to

$$|\boldsymbol{\epsilon}\cdot\boldsymbol{P}_{cv}|^2 = \frac{1}{3}(p_x^2 + p_y^2 + p_z^2) \tag{26}$$

where p_i is the i component of $\boldsymbol{P}_{cv}$. However, for superlattice structures, the symmetry is lowered by the superstructure layering which causes the direction to become preferred over the other two. This asymmetry leads to a momentum matrix element factor of the form

$$|\boldsymbol{\epsilon}\cdot\boldsymbol{P}_{cv}|^2 = \frac{1}{2}(1-\theta)(p_x^2+p_y^2)+(\theta)p_z^2 \tag{27}$$

where θ is 1 or 0 for the electric field polarization being perpendicular (TM) or parallel (TF) to the superlattice layers, respectively.

In Fig. 10 theoretical and experimental values (37) for the index of refraction of GaAsAl$_{0.3}$Ga$_{0.7}$–As superlattice at 300 K for both parallel and perpendicular polarizations at the Γ-point are presented. The superlattice has a well thickness L_z of 70 Å and a barrier thickness L_B of 75 Å. In Fig. 10(a) the results for the hybrid model include only the continuum exciton contribution (see Eqs. 24–25). The peaks on the parallel polarization curves correspond to the quantized *e*-hh(1) and *e*-lh(1) transitions, while for perpendicular polarization, only the *e*-lh(1) is present. The quantized hh transitions are absent for perpendicular polarization due to symmetry considerations [see Eq. (27)]. The peaks on the parallel polarization curves correspond to the quantized *e*-hh(1) and *e*-lh(1) transitions, while for perpendicular polarization, only the *e*-lh(1) is present. The quantized hh transitions are absent for perpendicular polarization due to symmetry considerations [see Eq. (27)]. As can be seen from Fig. 10(b), which contains the contribution of the bound exciton (Eqs. 22–23) the sharp rises in the experimental data correspond to bound exciton peaks. By comparing Figs. 10(a) and 10(b), one sees that the bound peaks rise more quickly and have a larger magnitude than the continuum peaks because excition effects are stronger for the bound case. The two figures also show that the bound exciton contribution increases the birefringence and for parallel polarization, for example, causes the appearance of four sets of peaks instead of two, i.e., bound and continuum peaks for *e*-h(1) and *e*-lh(1). Most important, Fig. 10(b) gives support

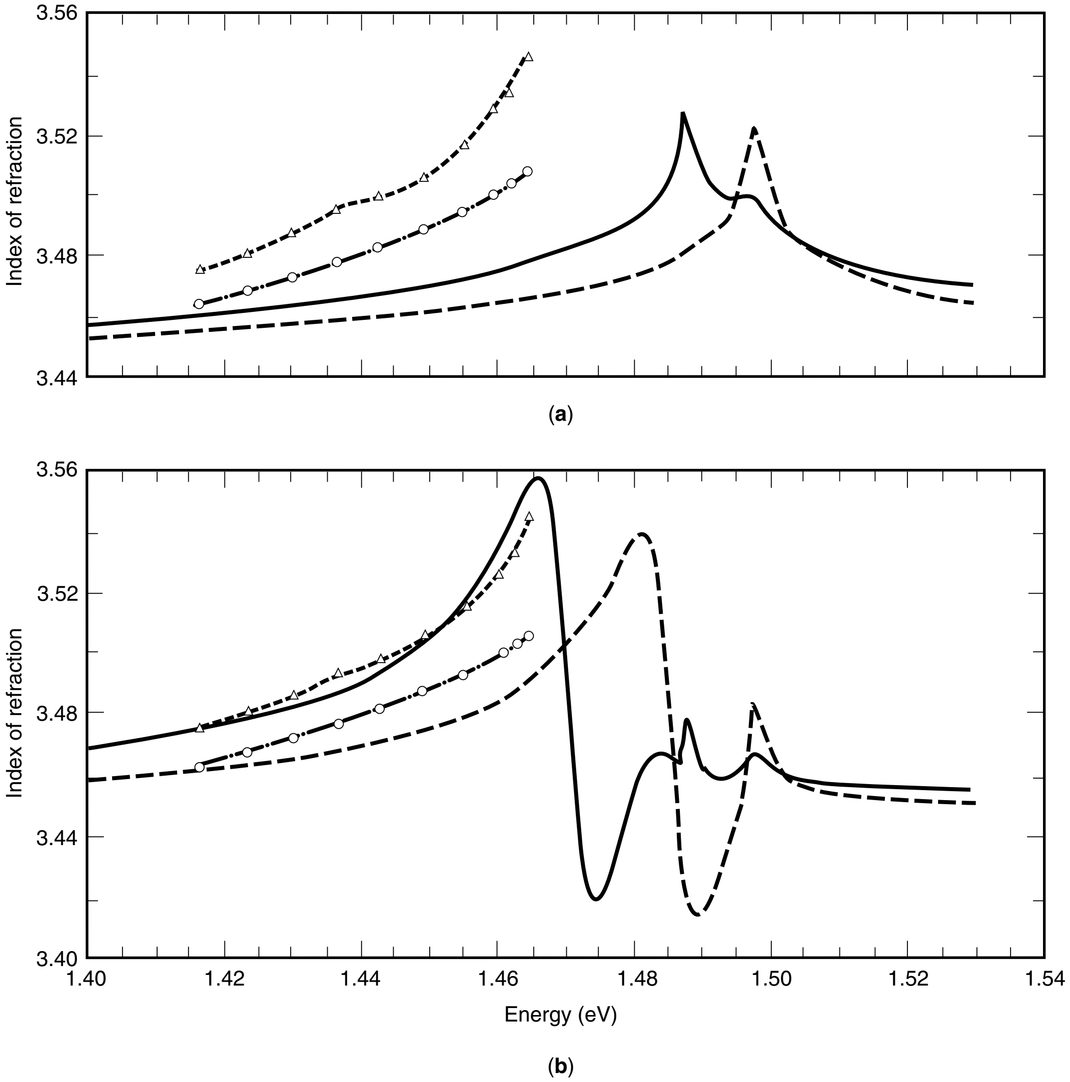

Figure 10. Index of refraction of a GaAs–Al$_{0.3}$Ga$_{0.7}$As superlattice around E_o. The dashed and dotted-dashed lines are the experimental results for parallel and perpendicular polarizations, respectively, while the solid and dotted lines are the results of our current model for parallel and perpendicular polarizations, respectively. In (a) these lines include only the continuum exciton contribution and in (b) they include both the continuum and bound exciton contributions.

for the validity of the model by the very good agreement between the theoretical and experimental curves. The only adjustable parameters in the model are the light hole effective mass $m_{lh} = 0.23\ m_o$, which was adjusted to obtain the correct energy for the $n = 1$ lh exciton peak, and the Lorentzian broadening parameter $\gamma = 3.5$ meV, which was chosen to obtain good agreement between the two parallel polarization curves while being in the line with the experimental estimates. As stated previously, the lh mass is in good agreement with the experimental value of Mann et al. (38), while the value for γ is very close to the suggested experimental value of Chemla et al. (39) of approximately 3 meV.

There are a couple of other interesting features to gather from Fig. 10(b). The sharp decrease in the exciton peaks is the result of the Kramers-Kroenig transformation of the quasi-2D exciton absorption peaks which resemble broadened energy delta functions. Experimentally, this effect might be difficult to detect due to strong absorption around the peaks causing the loss of signal in this energy range. The slight dip in the theoretical parallel polarization curve for $\hbar\omega \sim 1.485$ eV is due to the contribution of the bound lh exciton peak which is decreasing in this energy range. Again, as a result of absorption effects, this dip is probably not experimentally resolvable.

As already pointed out earlier there are also important excitonic effects at E_1, $E_1 + \Delta_1$. The exciton in this region has a large binding energy ($\approx$ 150 meV to 250 meV) which is due to the fact that it is essentially two-dimensional (bands are almost flat along $\langle 111 \rangle$) and the perpendicular masses are large compared to the masses at E_0, as shown in Table 1. Generally, semiempirical band structure calculations have adjusted their parameters so that the calculated E_1, $E_1 + \Delta_1$ peaks agree with the experiment "E_1, $E_1 + \Delta_1$" features. However, this is not quite correct since the experimental "E_1, $E_1 + \Delta_1$" features are lower than the band-to-band E_1, $E_1 + \Delta_1$ features by the 2D exciton binding energy of 150 meV to 250 meV. These 2D exciton binding energies have been evaluated in Y. Petroff and M. Balkanski (40), and more recently in T. Holden et al. (41).

BIBLIOGRAPHY

1. R. Dingle, Applications of Multiquantum Wells, Selective Doping, and Superlattices, in R. K. Williardson and A. C. Beer (eds.), *Semiconductors and Semimetals,* Vol. 24, New York: Academic Press, 1987.
2. J. I. Pankove, *Optical Processes in Semiconductors,* New York: Dover, 1971.
3. S. W. Kirchoefer et al., *Appl. Phys. Lett.,* **40**: 821, 1982.
4. Y. Suzuki and H. Okamoto, *J. Electronic Mater.,* **12**: 397, 1983.
5. N. Holonyak, Jr., et al., *Appl. Phys. Lett.,* **39**: 102, 1981.
6. F. Bassani and G. P. Parravicini, *Electronic States and Optical Transitions in Solids,* Oxford, UK: Pergamon, 1975, Chap. 5.
7. J. D. Jackson, *Classical Electrodynamics,* 2nd ed., New York: Wiley, 1975.
8. E. O. Kane, in R. K. Williardson and A. C. Beer (eds.), *Semiconductors and Semimetals,* Vol. 1, New York: Academic Press, 1966, p. 71.
9. K. B. Kahen and J. P. Leburton, *Phys. Rev. B,* **32**: 5177, 1985.
10. J. R. Chelikowsky and M. L. Cohen, *Phys. Rev. B,* **14**: 556, 1976.
11. M. Cardona, in E. Burstein (ed.), *Proc. Int. School Phys. "Enrico Fermi",* New York: Academic Press, 1972, p. 514.
12. P. O. Löwdin, *J. Chem Phys.,* **19**: 1396, 1951.
13. D. J. Chadi, *Solid State Commun.,* **20**: 361, 1976.
14. D. J. Chadi, *Phys. Rev. B,* **16**: 3572, 1977.
15. G. Dresselhaus, A. F. Kip, and C. Kittel, *Phys. Rev.,* **98**: 368, 1955.
16. D. E. Aspnes and A. A. Studna, *Phys. Rev. B,* **27**: 985, 1983.
17. B. Velicky and J. Sak, *Phys. Status Solidi,* **16**: 147, 1966.
18. W. Hanke and L. J. Sham, *Phys. Rev. B,* **21**: 4656, 1980.
19. D. E. Aspnes, *Phys. Rev. Lett.,* **31**: 230, 1973.
20. J. R. Chelikowsky and M. L. Cohen, *Phys. Rev. Lett.,* **31**: 1582, 1973.
21. C. Hermann and C. Weisbuch, *Phys. Rev. B,* **15**: 823, 1977.
22. D. R. Penn, *Phys. Rev.,* **128**: 2093, 1962.
23. B. R. Nag, in H. J. Queisser (ed.), *Electron Transport in Compound Semiconductors,* Vol. II, New York: Springer, 1980, p. 52.
24. J. M. Ziman, *Models of Disorder,* Cambridge, UK: Cambridge Univ. Press, 1977.
25. G. Bastard, *Wave Mechanics Applied to Semiconductors Heterostructures,* Paris, France: Les Editions de Physics, 1988.
26. G. A. Sai-Halasz, R. Tsu, and L. Esaki, *Appl. Phys. Lett.,* **30**: 651, 1977.
27. Y. C. Chang and J. N. Shulman, *Phys. Rev. B,* **31**: 2056, 1985.
28. D. F. Blossey, *Phys. Rev. B,* **10**: 3976, 1970.
29. R. L. Greene, K. K. Bajaj, and D. E. Phelps, *Phys. Rev. B,* **29**: 1807, 1984.
30. M. Shinada and S. Sugano, *J. Phys. Soc. Jpn,* **21**: 1936, 1966.
31. B. A. Vojak et al., *Solid State Commun.,* **35**: 477, 1980.
32. N. Holonyak, Jr., private communication.
33. W. D. Laidig, D. K. Blanks, and J. F. Schetzina, *J. Appl. Phys.,* **56**: 1791, 1984.
34. H. C. Casey, Jr., D. D. Sell, and M. B. Panish, *Appl. Phys. Lett.,* **24**: 63, 1974.
35. H. Okumura et al., *Appl. Phys. Lett.,* **46**: 377, 1985.
36. R. G. Hunsperger, *Integrated Optics: Theory and Technology,* Vol. 35, New York: Springer, 1982.
37. G. J. Sonek et al., *Proceedings of the Topical Meeting on Integrated and Guided Wave Optics,* Atlanta, GA, 1986, p. 18.
38. J. C. Mann et al., *Phys. Rev.,* **B30**: 2253, 1984.
39. D. S. Chemla et al., *IEEE J. Quantum Electron.,* QE-20, 265, 1984.
40. Y. Petroff and N. Balkansky, *Phys. Rev.,* **B3**: 3299, 1971.
41. T. Holdren et al., *Phys. Rev.,* **B56**: 4037, 1997.

Jean-Pierre Leburton
University of Illinois at Urbana-Champaign